



Optimized helical intermedium-period fiber grating for breathing monitoring

CHENXU LI,^{1,2} SHEN LIU,¹  JUNLAN ZHONG,^{1,*}  TAO ZOU,¹
WENQI YAN,¹ QIAO LIN,¹ YUELIANG XIAO,¹ AND YIPING WANG¹ 

¹Shenzhen Key Laboratory of Photonic Devices and Sensing Systems for Internet of Things, Guangdong and Hong Kong Joint Research Centre for Optical Fibre Sensors, Shenzhen University, Shenzhen 518060, China

²Department of Automotive Application Technology, Shangqiu Institute of Technology, Shangqiu 476000, China

*zhongjunlan@email.szu.edu.cn

Abstract: The investigation into the spectral properties and refractive index (RI) sensitivities at low RI region of helical intermedium-period fiber gratings (HIPFGs) with varied periods ranging from 10–48 μm is presented in detail for the first time. The structure of HIPFG is optimized for RI sensing in the RI range of 1.3–1.33 by comparing the optical properties of HIPFGs with different grating periods. The HIPFG with optimized structure is demonstrated to have a high average sensitivity of 302.5 nm/RIU in the RI ranging from 1.3 to 1.33, which is two orders more elevated than the traditional long-period fiber gratings. The improved HIPFG is also experimentally applied to breath monitoring in different states. Normal breath, slow breath, fast breath, and unhealthy breath are distinguished based on breathing rate, intensity, and time of exhalation and inhalation. The fastest response time is determined to be 10 ms. The results demonstrate that the optical fiber's sensitivity in the low RI region can be increased by shortening its period, offering a special strategy for improving detection performance of HIPFGs. By verifying its performance in breathing monitoring, it is proved that the optimized HIPFG sensor has the great potential to expand medical applications.

© 2024 Optica Publishing Group under the terms of the [Optica Open Access Publishing Agreement](#)

1. Introduction

Optical fiber sensors (OFSs) are a kind of sensing device based on the principle of utilizing an optical fiber to transmit or reflect light from a source to a modulator. They have become an increasingly prevalent rapid sensing technique because they have a number of benefits, such as high-quality factor (Q value), low volume mode, quick response, and easy integration [1–6]. Furthermore, the diversity of their forms encourages the use of fiber optic sensors in the analysis of numerous biological materials such as viruses, proteins, nucleic acids, and other life signs such as respiration, pulse, and blood pressure [7–12]. Therefore, OFSs, such as optical fiber gratings (OFGs) [11,12], photonic crystal fiber (PCF) [13,14], surface plasmon resonance (SPR) [15,16], Fabry-Perot interferometer (FPI) [17,18] and optical whispering gallery mode (WGM) [19,20,2], are ideal for a wide variety of biological applications, providing powerful instruments for scientific study and medical diagnostics.

Long period fiber grating (LPFG) is a passive device that forms a periodic refractive index modulation by inducing a periodic spatial structural distribution inside the core and cladding of the fiber. LPFGs are renowned for their exceptional sensitivity to changes in refractive index (RI), primarily owing to the remarkable characteristic of their evanescent field, which deeply penetrates into the surrounding environment [21]. In addition to their high RI sensitivity, LPFGs offer a range of advantages, including minimal insertion loss, affordability, and compact dimensions. These attributes make LPFGs a highly desirable and versatile tool in various applications, from sensing to telecommunications and beyond [11,22,23]. A significant portion of recent research has focused on enhancing the sensitivity to specific measurements or reducing the cross-sensitivity

to other factors because it is essential to the development of fiber grating's potential biosensing applications. In the quest to enhance the RI sensitivity of optical fibers, several key strategies are commonly employed. Among these, the utilization of the fiber cladding mode dispersion inflection point, the reduction in the diameter of the fiber cladding, and the application of high refractive index films onto LPFGs stand out as major approaches.

The grating design has a very high RI sensitivity when the coupled cladding mode and grating period are at or near the dispersion turning point. For example, a LPFG created by Pilla et al. showed extremely high RI sensitivity, reaching 9100 nm/RIU at RI of 1.3469 [24]. Liu et al. [23] studied the RI sensing characteristics of the long-period fiber grating with dispersion turning point written in boron-germanium co-doped single-mode fiber (SMF). The RI sensitivity of the grating is 13497.7 nm/RIU when RI varying from 1.447 to 1.453. However, when the coupling mode is at or near the inflection point of dispersion, the LPFG is also sensitive to other non-target parameters, such as changes in temperature and pressure, among others. This sensitivity can lead to significant crosstalk, where these unrelated factors can interfere with or affect the intended measurement or signal transmission [25–26]. In 2015, Fu et al. [27] prepared asymmetric LPFG on a thin-core fiber with a core diameter of only 1.8 μm , and achieved 1047.3 nm/RIU within the refractive index range of 1.400-1.440. The high sensitivity verifying that reducing the diameter of the fiber cladding can effectively improve the response of the LPFG to the external environment. Furthermore, coating the surface of a fiber grating is another way to increase its RI sensitivity. Davies et al. [28] prepared titanium dioxide (TiO_2)/silicon dioxide (SiO_2) nano-films on the surface of long-period fiber gratings by sol-gel method. This method obviously improves the refractive index sensitivity of LPFG in the range of 1.42-1.44 refractive index. For refractive index (RI) sensing, Nidhi et al. [29] presented an LPFG coated with Indium Tin Oxide (ITO) film. The results showed that the RI sensitivity was increased by a factor of 2-3 for glycerol solutions with RI ranging from 1.3490 to 1.4198. The LPFG-based sensors are widely investigated in various fields because of their merits of high sensitivity, minimal insertion loss, compact dimensions, and beyond. Most of these researches are focused on the improvements of sensing performances in high RI regions, commonly above 1.33. However, the lower RI region contains a wealth of valuable life information. The development of an LPFG with high sensitivity in RI lower than 1.33 is vital for the expansion of LPFG-based applications.

In this work, we propose a helical intermedium-period fiber grating (HIPFG) with the optimized structure to solve the problem of poor sensitivity of traditional LPFGs when the sample RI is located in the range of 1.3-1.33. The results demonstrates the HIPFG with an optimized period has greater sensitivity in the low RI range. Also, this work verifies that by changing the grating period, the LPFG working RI region with high sensitivity can be obtained. Finally, the optimized HIPFG is applied for breathing monitoring to verify its application potential in biosensing. This work encompasses a comprehensive exploration of HIPFGs with a diverse range of periods spanning from 10 to 48 μm . These intricate grating structures are meticulously inscribed into single-mode fiber (SMF) and elliptical core fiber (ECF) utilizing a highly efficient hydrogen-oxygen flame heating system, ensuring precise and controlled fabrication. Then, the spectrum properties and sensitivities of these HIPFGs' low RI area are following thoroughly investigated for refining and improving the grating structure. Last, the practical utility of these improved HIPFGs as sensing devices is rigorously assessed, with a particular focus on their applicability in breath monitoring. Through a series of meticulously designed experiments, the sensing properties of these advanced HIPFGs are empirically validated.

2. Sample fabrication

A high-efficiency hydrogen-oxygen flame heating system, which included a high-precision rotator, two translation stages, and a hydrogen generator, was used to create HIPFGs. The structure diagram is presented in Fig. 1. In the fabrication process, the optical fiber is twisted under molten

conditions. When the optical fiber leaves the flame area, it cools rapidly and the stress is released, leading to the spatial refractive index modulation of the cladding and core. This system has a number of benefits, including high processing yield, high efficiency, and the ability to quickly fabricate high-quality HIPFGs with various periods [10–12, 30,]. To process HIPFGs with wide period range, we choose to process a periodic modulation structure in single-mode fiber (SM-28) and elliptical core fiber (P1C0027901B0, YOEC), provided by Yangtze Optical Electronic Co., Ltd. (Wuhan, China). The HIPFGs inscribed into SMF and ECF are defined as S-HIPFG and E-HIPFG, respectively.

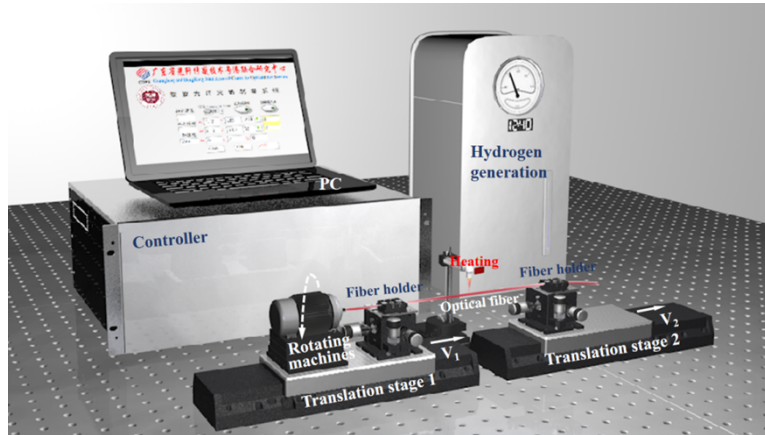


Fig. 1. Structure diagram hydrogen-oxygen flame heating system.

Five HIPFG samples (S-HIPFG-1, S-HIPFG-2, E-HIPFG-3, E-HIPFG-4, and E-HIPFG-5) were processed by the hydrogen-oxygen flame heating system. When translation speed of right stage 1 and 2 are defined V_1 and V_2 , respectively and the stepper motor's operating speed is defined to be Ω , the S-HIPFG's pitch can be calculated by the following formula [10–12,30]:

$$\Lambda = 60V_2/\Omega \quad (1)$$

The ECF's two-fold axial symmetry, which has built-in major and minor axis structures, allows us to calculate the period of the E-HIPFG grating using the formula $\Lambda=30V_2/\Omega$. This period is half of period of the S-HIPFG produced using the same system parameters. According to the formula, we can get HIPFGs with various periods by changing the motor's rotational rate and the translation speed. The precision cutting device cuts the sample to the optimal length in accordance with the ideal coupling scenario, which should bring the coupling strength of the sample reasonably close to the theoretical ideal coupling length. The connection between the light source and detector was made by splicing the HIPFGs with two conventional SMFs.

A helical long period grating sample (S-HLPFG-A) based on SMF was prepared in order to compare the RI sensitivity of regular HLPFG and HIPFG. All sample fabrication parameters and structure details are presented in Table 1. As the period of the grating becomes smaller, the length of the grating becomes smaller and smaller samples provide less flexibility and integrability. The grating length of the E-HIPFG is approximately 3 mm, which is an order of magnitude smaller than the lengths of S-HIPFG. The micrographs corresponding to the five groups of gratings are shown in Fig. 2(a-e), according which the variation law of the grating period can be clearly seen. The core size decreases when the HIPFG is inscribed into the SMF or ECF, which is related to the energy of the hydrogen-oxygen flame and the rotation motor's and translation stages' working speeds. Furthermore, as seen in Fig. 2(a-e), periodic deforms are visible in the side views of the

cores. Compared to the SMF, the differences in the helical structure are more visible in the ECF due to its two-fold axial symmetry.

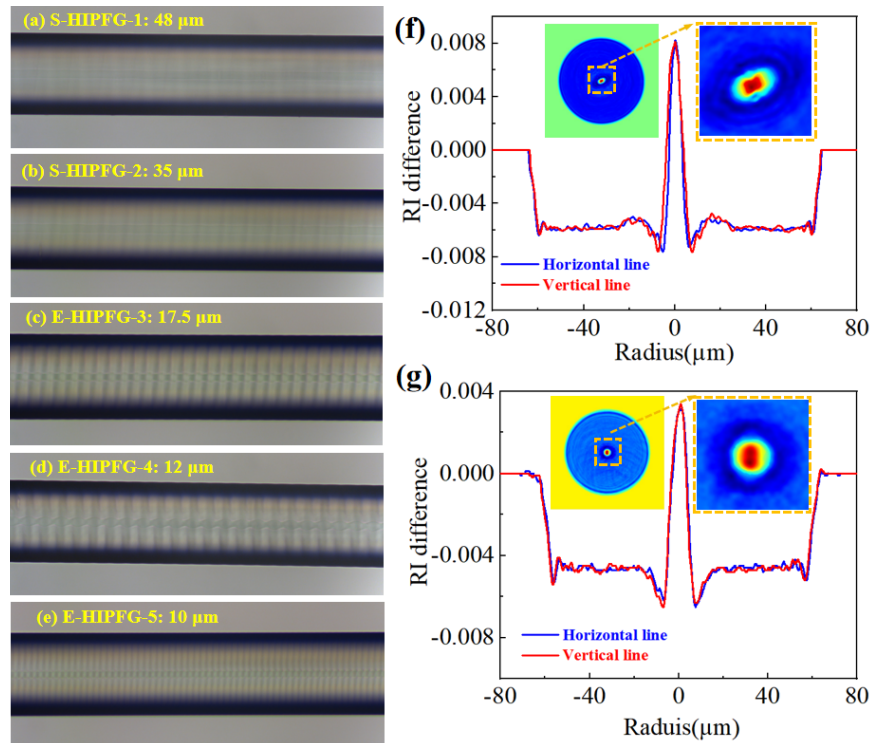


Fig. 2. (a-e) The microscope images of HIPFG samples. (f-g) Refractive index distribution diagram of unprocessed elliptical core optical fiber end face and E-HIPFG-3 end face.

Table 1. The processing parameters and structural details of HIPFGs.

Sample number	Fiber type	Processing parameters	Period (um)	Length (mm)
S-HLPFG-A	SMF	$V_1 = 1.1$ mm/s, $V_2 = 1.2$ mm/s, $\Omega = 103$ rpm	699	20.0
S-HIPFG-1	SMF	$V_1 = 1.1$ mm/s, $V_2 = 1.2$ mm/s, $\Omega = 1500$ rpm	48	16.0
S-HIPFG-2	SMF	$V_1 = 1.1$ mm/s, $V_2 = 1.2$ mm/s, $\Omega = 2057$ rpm	35	17.5
E-HIPFG-3	ECF	$V_1 = 1.1$ mm/s, $V_2 = 1.2$ mm/s, $\Omega = 2057$ rpm	17.5	2.5
E-HIPFG-4	ECF	$V_1 = 1.1$ mm/s, $V_2 = 1.2$ mm/s, $\Omega = 3000$ rpm	12	4
E-HIPFG-5	ECF	$V_1 = 0.9$ mm/s, $V_2 = 1.0$ mm/s, $\Omega = 3000$ rpm	10	3

A three-dimensional fiber refractive index analyzer (SHR-1602) was used to assess the raw ECF (ECF13-125-U25, YOEC) and the E-HIPFG-3 (17.5 m) to compare the refractive index distribution of the end face of the elliptical core fiber before and after twisting. Only the modifications in the core of ECF fiber are examined here because the core of single-mode fiber does not change appreciably before and after HIPFG inscribed into. The test temperature is 18.7 °C and humidity is 61.5%. The matching oil's refractive index is 1.4643. The unprocessed ECF's refractive index distribution is elliptical, with the core's maximum relative value being +0.00822 and its absolute RI being 1.47252, while the cladding's relative RI is roughly -0.006 and its absolute RI is 1.4583, as shown in Fig. 2(f). For the unprocessed ECF, there is a 0.01422 RI difference between the core and cladding. Figure 2(g) illustrates the end-face RI distribution

of E-HIPFG-3, which is more resemblant of a circle than that of the unprocessed one's. The fiber core has an absolute refractive index of 1.4677 and the relative refractive index of +0.00340. The cladding's absolute RI is 1.4596, but its relative refractive index is -0.00474. The cladding and fiber core have a 0.00814 refractive index difference. It is evident that the refractive index (RI) of the fiber core after the HIPFG inscribed into it reduces by 0.00542 when compared to that of the unprocessed ECF, the cladding refractive index rises by 0.00126.

3. Optical properties

HLPFG and HIPFG are typically created by periodically changing the refractive index of the fiber cladding or core. When only the first-order diffraction order is taken into account, the resonance wavelength λ of the coupling of the fundamental mode and the co-propagating cladding mode can be written as [31–32]:

$$\lambda = (n_{co}^{eff} - n_{cl,m}^{eff})\Lambda, \quad (2)$$

where n_{co}^{eff} and $n_{cl,m}^{eff}$ are the effective refractive index of the core mode and the m th cladding mode, respectively. From Eq. (1), the effective refractive indices of the core and cladding as well as the grating period are what control the resonance wavelength of the HLPFG/HPFG. We measured the spectra of HIPFGs/HLPFG with the intent of analyzing the spectral changing trend with a period variation. An amplified spontaneous emission source (ASE, NKT Photonics) and an optical spectrum analyzer (OSA, YOKOGAWA, AQ6370C) with a resolution of 0.02 nm are used to record the transmission spectra of the fabricated HIPFGs.

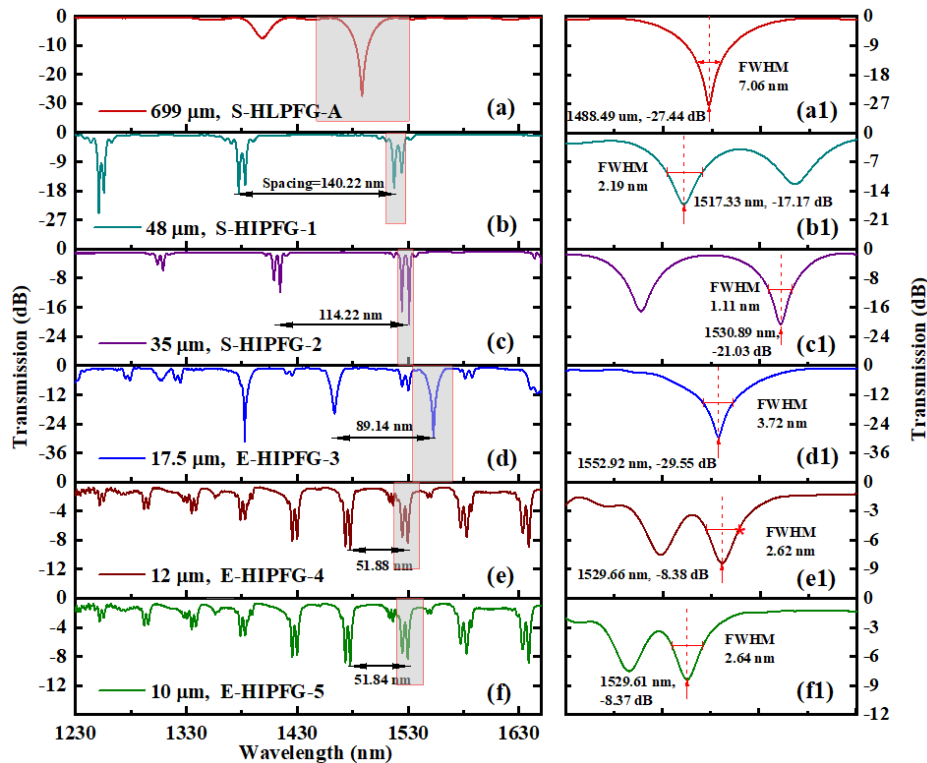


Fig. 3. (a-f) Transmission spectra of HIPFG samples in air; (a1-f1) enlarged views of the peaks in the wavelength range around 1530 nm.

The HIPFG is fixed at both ends by two stages during the measurement process, leaving the grating in a naturally stretched state. The record wavelength range is 1230-1650 nm, as shown in Figs. 3(a-f). And Figs. 2(a1-f1) exhibits enlarged views of the peaks in the wavelength range around 1530 nm, as shown with the gray area of Figs. 3(a-f), respectively. The resonance peaks of HIPFGs/HLPFG appear as dual resonances, which are caused by the difference in the effective RI of the TM (transverse magnetic) and TE (transverse electric) cladding modes, which increases with the launch wavelength and cladding mode order [31,32]. The double-peak characteristic of 17.5 μm HIPFG is not immediately apparent. This is caused by the degeneracy of the TE and TM modes because of the very short distance between these modes. That is, the TM-peak and TE-peak overlap, and the intensity of the analogous single peak of the 17.5 μm -HIPFG is the superposition of these two peaks, resulting in higher peak intensity and FWHM when compared to other samples.

The resonant mode order m of shorter HIPFGs/HLPFG present in the detection spectral region is higher than that of longer ones. Therefore, the coupling strengths of the dual peaks decrease as the grating period decreases because the shorter fiber grating has higher m and the overlap between the core and cladding field distributions decreases in this case [32]. At the same time, the wavelength interval between modes also decreases as the order increases, which is good agreement with our experimental date: as the grating pitch is reduced from 48 μm to 10 μm , the spacing between adjacent resonance peaks decreases from 140.22 nm to 51.84 nm, the details are presented in Table 2. Therefore, the number of resonant peaks of HIPFGs is more than that of traditional HLPFG. There is only one dual-dip in the spectrum of HLPFG, with the coupling strength of 27.44 dB and the full width at half maximum (FWHM) of 7.06 nm. HIPFGs have a lower coupling strength, but their FWHM are about 1-4 nm, which are much smaller than that of HLPFGs, as listed in Table 2.

Table 2. The comparison of optical features of HIPFGs.

Sample No.	Spacing (nm)	Maximum Intensity (dB)	FWHM (nm)	$S_{\text{RI}-1.3-1.33}$ (nm/RIU)
S-HLPFG-A	-	27.44	7.06	4.6
S-HIPFG-1	140.22	17.17	2.19	101.8
S-HIPFG-2	114.22	21.03	1.11	108.8
E-HIPFG-3	89.14	29.55	3.72	149.5
E-HIPFG-4	51.88	8.38	2.62	302.5
E-HIPFG-5	51.84	8.37	2.64	-

4. RI sensing characteristics

HIPFGs capabilities for RI sensing are evaluated by put HIPFGs into RI matching liquid with different RI values. During the measurement process, both ends of the HIPFG are also fixed. Then a wiped glass is placed on the lifting platform, and slowly rises until it just touches with the grating sample. The RI matching liquid (Cargille Labs) to cover the HIPFG sample completely for the measurement. After every measurement, the lifting platform is lowered, and the glass slide and grating sample is cleaned by alcohol to until the spectrum back to the original state. Then we replace the RI matching liquid with different RI values, and repeat the previous steps.

The surrounding refractive index (SRI) sensitivity of LPFG is determined by [32,34]:

$$\frac{d\lambda_{res}}{dn_{sur}} = \lambda_{res} \cdot \gamma \cdot \Gamma_{sur}, \quad (3)$$

γ refers the general sensitivity factor and is defined by

$$\gamma = \frac{\frac{d\lambda_{res}}{d\Lambda}}{n_{co}^{eff} - n_{cl,m}^{eff}}, \quad (4)$$

and Γ_{sur} is describe the surrounding RI dependence of the waveguide dispersion and are defined by

$$\Gamma_{sur} = \frac{u_m^2 \lambda_{res}^3 n_{sur}}{8\pi r_{cl}^3 n_{cl} (n_{co}^{eff} - n_{cl,m}^{eff}) (n_{cl}^2 - n_{sur}^2)^{3/2}}, \quad (5)$$

where u_m is the m th root of the zeroth-order Bessel function of the first kind, and r_{cl} and n_{cl} are the radius and refractive index of the fiber cladding, respectively. According to the formulas, the detection sensitivity will improve in the long wavelength region and high RI because the sensitivity factor γ rises with increasing mode order and effective RI [32,21]. At same time, at the same or adjacent resonance wavelength, the shorter the grating period, the higher order mode exists and the higher the sensitivity can be obtained.

Figure 4 shows the variation of the wavelength shift of HIPFGs/HLPFG with RI. Among them, after the 10- μm HIGPF (E-HIPFG-5) is added with the RI matching liquid, its the resonance peaks became ambiguous. This phenomenon is caused by the fact that when the grating period is less than 10 μm , the effective refractive index of the cladding mode is less than 1.3, and a phase matching condition is dissatisfy in the wavelength of 1230-1650 nm when the surrounding refractive index is higher than 1.3. Specially, the resonant wavelength of HLPFG drifts with the refractive index in the opposite direction from other HIPFGs due to the longer grating period and lower mode order in the detection spectrum area [32]. The drift's direction is altered to match that of other HIPFGs in order to more accurately compare the drift's magnitude. Figure 4(a) illustrates that as the period reduces, the maximum refractive index value that the grating can measure decreases. The maximum refractive index values measured from large to small periods are approximately 1.454, 1.424, 1.410, 1.370, and 1.325, respectively. The sensitivity fitting curve also experiences exponential change. Regular HLPFG are more sensitive in high-RI solutions, whereas HIPFGs are more sensitive in low-RI ranges. Figure 4(b) shows a enlarged diagram of the resonance wavelength shift of HIPFGs/HLPFG in the lower refractive index range (RI = 1.30~1.33). The full lines are the Boltzmann fitting lines. The sensitivity of HIPFGs/HLPFG increases with the decrease of the grating period. The corresponding average sensitivities ($S_{ave(1.3-1.33)}$) in this range are 4.6, 101.8, 108.8, 149.5 and 302.5 nm/RIU, as listed in Table 2.

By comparing the spectral properties and RI detection performance of HIPFGs/HLPFG with different periods, we draw the following conclusions: First, all peaks of HIPFGs/HLPFG appear in the form of dual-peaks. Compared with HLPFG, the peak-to-peak spacing of HIPFGs is smaller, because HIPFGs has a higher mode number in the same detection spectral range. Moreover, HIPFGs have a smaller FWHM, which is beneficial to improve the detection resolution. Second, the smaller the period of the grating, the smaller the maximum RI value it can detect, but the higher its sensitivity in the RI range of 1.3-1.33. Among them, when the period is 12 μm , the average sensitivity reaches the maximum, which is 302.5 nm/RIU. Third, when the spiral grating period is lowered to 10 μm , there is no discernible resonance peak in the wavelength range of 1230-1650 nm when the surrounding RI is more than 1.3. This is due to the grating's effective RI being less than 1.3, and the phase matching condition is dissatisfied in the wavelength range of 1230-1650 nm. Therefore, we believe that HIPFG with a period of 12 μm is the most suitable for breath detection.

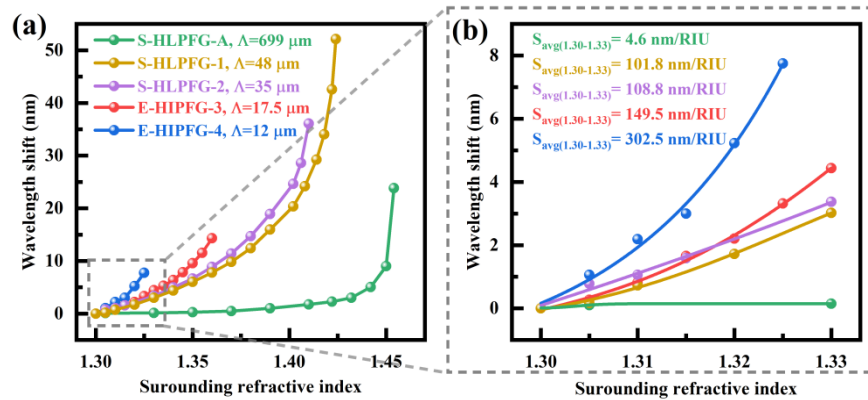


Fig. 4. The resonant wavelength shift of five groups of helical fiber grating samples with the change of refractive index (b) The magnified diagram of the resonant wavelength drift of RI = 1.30~1.33, with Boltzmann fitting line.

5. Breathing monitoring

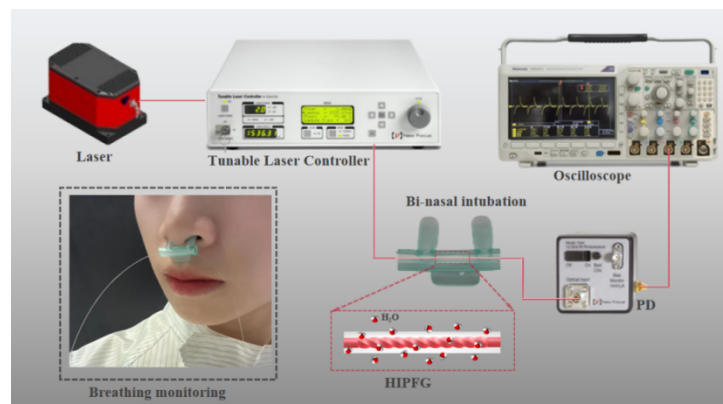


Fig. 5. The breath experiment setup, the inset figure illustrates the state of the Bi-nasal intubation connected to the volunteer's nose.

To further evaluate the potential bio-application of the optimized HIPFG sensor, we employ the E-HIPFG-4 for breathing monitoring based on the difference in humidity between indoor air (30–60% RH) and nasal exhalation (about 70–90% RH) [33]. A testing system with a tunable laser (NewFocus TLB-6700), photodetector (PD, NewportModel 1544-B), and oscilloscope (Tektronix, MDO3054) was utilized to monitor the volunteers' breath in different statuses. The experimental setup is illustrated in Fig. 5. During the measurement, the E-HIPFG-4 was fixed in bi-nasal intubation to minimize the variation cause by airflow during breathing. In addition, we previously showed that HIPFG is resistant to torsion, stress, and temperature [10–11], the peak changes in airflow caused by breathing can be overlooked. Then, the bi-nasal intubation is connected to the volunteer's nose, as shown in the inset figure of Fig. 5. The laser wavelength was set at 1535.81 nm, the right half-peak value of resonance peak of the peak, shown as a star in Fig. 3(e). The intensity varied at 1535.81 nm was monitored with inhaled and exhaled human breath at room temperature. Utilizing the half-peak value has the benefit of allowing for a more accurate analysis of the breathing state because it can determine if the resonance dip is redshifted

or blueshifted based on an decrease or increase in intensity. The intensity decreasing refers to the redshift of the resonance dip and the rise of the environmental humidity, which means the exhale state of the breath. And vice versa, increasing of the intensity corresponds to the inhale state.

We measured and compared four breathing patterns among the volunteers, which included normal breathing, slow breathing, fast breathing, and congested breathing, as illustrated in Fig. 6. Two volunteers were engaged to record the breathing conditions. One healthy volunteer was tested for normal, slow, and fast breathing, while another volunteer suffering from a cold was tested for congested breathing under normal breathing conditions. Figures 6(a2-d2) depict a single breath cycle for each breathing pattern along with response time information for exhaling and inhaling. It is evident from the figures that the intensity decreases during inhalation (green area) in the negative direction and increases during exhalation (yellow area) in the positive direction. Different breathing states result in distinct manifestations of these amplitude and frequency changes.

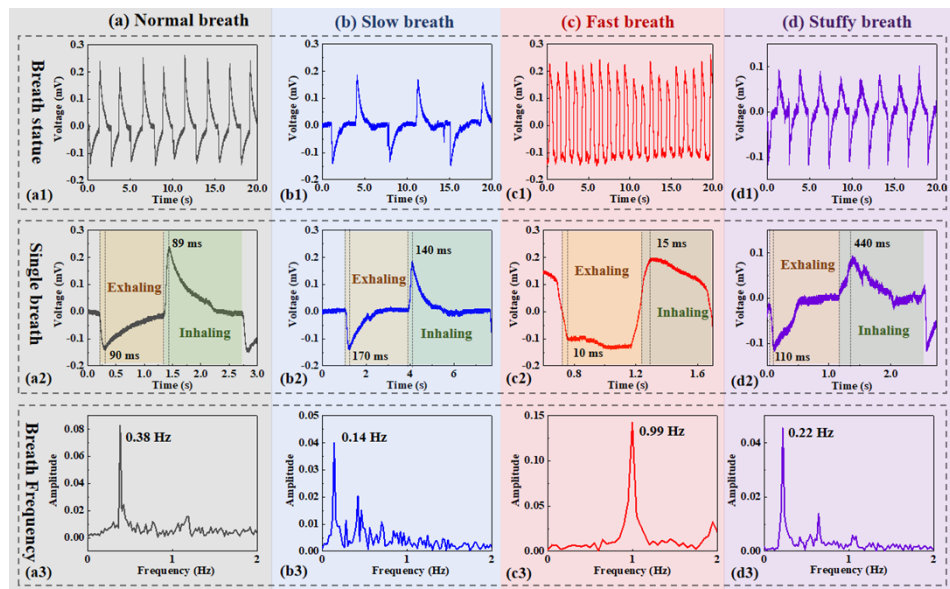


Fig. 6. The real-time response of the E-HIPFG-4 breath sensor, and their time responses in a single breath and breath frequency. (a) normal breath, (b) slow breath, (c) fast breath, (d) and stuffy breath.

By comparing across the spectrum of breath states, we analyze the dynamics of respiration. In the normal state, exhaling and inhaling exhibit response times of approximately 90 ms and 89 ms, respectively. This synchronized interplay highlights the balanced nature of regular breathing. Utilizing the power of Fast Fourier Transform (FFT) analysis, the respiration frequencies emerge with clarity, precisely quantifying at 0.38 Hz, as depicted in Fig. 6(a3). The slow breath state has a noticeable departure from the norm breath state. The elongated breath period contrasts starkly with the rapid tempo of normal respiration. As a result of this extended cycle, the breath frequency gracefully reduces to 0.14 Hz. The accompanying response times for exhaling and inhaling elongate accordingly, extending to 170 ms and 140 ms, respectively. Conversely, the fast breathing state also introduces a contrasting narrative, where both exhale and inhalation occur at a brisk pace, reflecting response times of 10 ms and 15 ms, respectively. This accelerated exchange of breath is mirrored by the breath frequency, surging to 0.99 Hz. With an increase in breath frequency, it is apparent that the response times of the breath sensor shorten, with the fastest response times for exhale and inhale being 10 ms and 15 ms, respectively. This might be the case

because the volunteer's nose-nearby humidity rises more quickly in a faster breath condition than it does in a slower one. Conversely, when the volunteers experienced congestion due to a cold, a perceptible shift occurred in their breathing patterns. The once-steady intensity and frequency of respiration noticeably diminished and grew increasingly erratic, as depicted in Fig. 6(d).

The results of the breathing monitoring experiment demonstrate that the HIPFG-based sensor has a relatively fast response time and can monitor respiration in real time. Additionally, when compared to previous breathing sensors, the HIPFG-based sensor can not only monitor a variety of breathing states but also identify the process of inhalation and exhalation in real-time, providing more information for clinical respiratory disease diagnosis and treatment. In previous studies [ref. 10,11], we showed that the HIPFG is insensitive to external disturbances such as temperature, twist, and stain, ensuring a low cross-sensitivity to external parameters for HIPFG in respiration sensing, which improves the accuracy of breathing monitoring. This multifaceted potential implies that the proposed sensor holds the promise of achieving not only elevated levels of resolution and accuracy but also real-time, multi-parameter breath monitoring capabilities, thus presenting a comprehensive solution for breath analysis.

6. Conclusion

The HIPFG-based breath sensor is proposed with an optimized grating structure. By comparing the HIPFGs with different grating periods, the optimized HIPFG of 12 μm -grating period and 4 mm-grating length is obtained. It has a high RI sensitivity of 302.5 nm/RIU in the RI range of 1.3–1.33, which is two orders high than the conventional LPFG. This result indicates that by fine-tuning the grating period of HIPFG, the sensitivity within the low RI range can be significantly enhanced, which provides a method for improving the RI sensitivity of fiber gratings with a simple preparation process and good sample repeatability. Then, the optimized HIPFG is undergoing breath monitoring tests to distinguish between various breath patterns like normal, slow, fast, and unhealthy breathing, based on factors such as breathing rate, intensity, and exhalation and inhalation timing. The fastest response time is 10 ms in fast breathing mode. In addition, HIPFG has the advantages of small size and considerable stability, promising great potential for achieving high-resolution, precise real-time, and portable breath monitoring, thus presenting a robust foundation for comprehensive breath analysis capabilities.

Funding. National Natural Science Foundation of China (62175165, 62305225); Shenzhen Science and Technology Program (JCYJ20210324120403009); Guangdong Basic and Applied Basic Research Foundation (2021A1515011834); Shenzhen Key Laboratory of Ultrafast Laser Micro/Nano Manufacturing (ZDSYS20220606100405013).

Disclosures. The authors declare no conflicts of interest.

Data availability. Data underlying the results presented in this paper are not publicly available at this time but may be obtained from the authors upon reasonable request.

References

1. B. Lee, "Review of the present status of optical fiber sensors," *Opt. Fiber Technol.* **9**(2), 57–79 (2003).
2. M. H. Jali, H. R. A. Rahim, M. A. M. Johari, *et al.*, "Optical characterization of different waist diameter on microfiber loop resonator humidity sensor," *Sens. Actuators, A* **285**, 200–209 (2019).
3. F. Wang, Y. Zhang, Y. Qu, *et al.*, "Improved Resolution of Temperature Sensor Using Fast and Slow Light in a Fiber Resonator," *IEEE Sens. J* **23**(5), 4825–4832 (2023).
4. G. Rajan, "Optical fiber sensors: advanced techniques and applications," CRC press (2017).
5. P. Lu, N. Lalam, M. Badar, *et al.*, "Distributed optical fiber sensing: Review and perspective," *Appl. Phys. Rev.* **6**(4), 041302 (2019).
6. J. Luo, S. Liu, P. Chen, *et al.*, "Highly sensitive hydrogen sensor based on an optical driven nanofilm resonator," *ACS Appl. Mater. Interfaces* **14**(25), 29357–29365 (2022).
7. Y. Yang, R. Zhao, Y. Wang, *et al.*, "Rapid and universal detection of SARS-CoV-2 and influenza A virus using a reusable dual-channel optic fiber immunosensor," *J. Med. Virol.* **94**(11), 5325–5335 (2022).
8. M. E. Bosch, A. J. R. Sánchez, F. S. Rojas, *et al.*, "Recent development in optical fiber biosensors," *Sensors* **7**(6), 797–859 (2007).
9. W. Bao, F. Chen, H. Lai, *et al.*, "Wearable breath monitoring based on a flexible fiber-optic humidity sensor," *Sens. Actuators, B* **349**, 130794 (2021).

10. S. Liu, W. Yan, J. Zhong, *et al.*, "Compact breath monitoring based on helical intermediate-period fiber grating," *Sens. Actuators, B* **369**, 132372 (2022).
11. J. Zhong, S. Liu, T. Zou, *et al.*, "All fiber-optic immunosensors based on elliptical core helical intermediate-period fiber grating with low-sensitivity to environmental disturbances," *Biosensors* **12**(2), 99 (2022).
12. J. Zhong, W. Yan, S. Liu, *et al.*, "Application of the Principal Components Analysis to Optical Fiber Sensor for Multiparametric Detection of Strain and Torsion," *J. Lightwave Technol.* **40**(22), 7439–7446 (2022).
13. W. C. Wong, C. C. Chan, L. H. Chen, *et al.*, "Polyvinyl alcohol coated photonic crystal optical fiber sensor for humidity measurement," *Sens. Actuators, B* **174**, 563–569 (2012).
14. B. Kaur, S. Kumar, and B. K. Kaushik, "Advances in photonic crystal fiber: sensing and supercontinuum generation applications," *Opt. Fiber Technol* **72**, 102982 (2022).
15. Y. Zhao, R. J. Tong, F. Xia, *et al.*, "Current status of optical fiber biosensor based on surface plasmon resonance," *Biosens. Bioelectron.* **142**, 111505 (2019).
16. B. Li, X. Yan, X. Zhang, *et al.*, "No-core optical fiber sensor based on surface plasmon resonance for glucose solution concentration and temperature measurement," *Opt. Express* **29**(9), 12930–12940 (2021).
17. T. Zhang, P. Pathak, S. Karandikar, *et al.*, "polymer nanostructured Fabry–Perot interferometer based biosensor," *Biosens. Bioelectron.* **30**(1), 128–132 (2011).
18. S. Tang, M. Zou, C. Zhao, *et al.*, "Fabry-Perot Interferometer Based on a Fiber-Tip Fixed-Supported Bridge for Fast Glucose Concentration Measurement," *Biosensors* **12**(6), 391 (2022).
19. L. Liang, M. Li, N. Liu, *et al.*, "A high-sensitivity optical fiber relative humidity sensor based on microsphere WGM resonator," *Opt. Fiber Technol.* **45**, 415–418 (2018).
20. X. Zhao, Z. Guo, Y. Zhou, *et al.*, "Optical whispering-gallery-mode microbubble sensors," *Micromachines* **13**(4), 592 (2022).
21. M. Gambhir and S. Gupta, "Review of turn around point long period fiber gratings," *J. Sens. Technol.* **5**(04), 81–89 (2015).
22. C. Colaço, P. Caldas, I. Del Villar, *et al.*, "Arc-induced long-period fiber gratings in the dispersion turning points," *J. Lightwave Technol.* **34**(19), 4584–4590 (2016).
23. Z. Liu, Y. Liu, C. Mou, *et al.*, "CO₂ laser-written long-period fiber grating with a high diffractive order cladding mode near the turning point," *Appl. Opt.* **57**(17), 4756–4760 (2018).
24. P. Pilla, C. Trono, F. Baldini, *et al.*, "Giant sensitivity of long period gratings in transition mode near the dispersion turning point: an integrated design approach," *Opt. Lett.* **37**(19), 4152–4154 (2012).
25. J. Tang, Z. Zhang, G. Yin, *et al.*, "Long period fiber grating inscribed in hollow-core photonic bandgap fiber for gas pressure sensing," *IEEE Photonics J.* **9**(5), 1–7 (2017).
26. Q. Wang, C. Du, J. Zhang, *et al.*, "Sensitivity-enhanced temperature sensor based on PDMS-coated long period fiber grating," *Opt. Commun.* **377**, 89–93 (2016).
27. C. Fu, X. Zhong, C. Liao, *et al.*, "Thin-core-fiber-based long-period fiber grating for high-sensitivity refractive index measurement," *IEEE Photonics J.* **7**(6), 1–8 (2015).
28. E. Davies, R. Viitala, M. Salomäki, *et al.*, "Sol-gel derived coating applied to long-period gratings for enhanced refractive index sensing properties," *J. Opt. A: Pure Appl. Opt* **11**(1), 015501 (2009).
29. R. S. Kaler and P. Kapur, "Enhancement of sensitivity of the refractive index using ITO coating on LPG," *Opto-Electron. Adv. Mater.-Rapid Comm.* **8**(1-2), 45–48 (2014).
30. T. Zou, J. Zhong, S. Liu, *et al.*, "Helical intermediate-period fiber grating for refractive index measurements with low-sensitive temperature and torsion response," *J. Lightwave Technol.* **39**(20), 6678–6685 (2021).
31. Z. Yan, H. Wang, C. Wang, *et al.*, "Theoretical and experimental analysis of excessively tilted fiber gratings," *Opt. Express* **24**(11), 12107–12115 (2016).
32. X. Shu, L. Zhang, and I. Bennion, "Sensitivity characteristics of long-period fiber gratings," *J. Lightwave Technol.* **20**(2), 255–266 (2002).
33. S. Kano, K. Kim, and M. Fujii, "Fast-response and flexible nanocrystal-based humidity sensor for monitoring human respiration and water evaporation on skin," *ACS Sens.* **2**(6), 828–833 (2017).
34. C. Xu, C. Jiang, and Y. Liu, "High diffraction order cladding modes of helical long-period gratings inscribed by CO₂ laser," *Appl. Opt.* **59**(10), 3086–3092 (2020).